Available online at www.sciencedirect.com

ScienceDirect

Physics Procedia 83 (2016) 634 – 646

Physics Procedia

9th International Conference on Photonic Technologies - LANE 2016

Possibility of multi-material laser cladding fabrication of nickel alloy and stainless steel

D. Kotoban[a,]*, A. Aramov[a], T. Tarasova[a]

[a]*Moscow State University of Technology "STANKIN", Vadkovsky per. 3a, 127055 Moscow, Russia.*

Abstract

There are some applications in the industry for multi-material components, including device engineering and multifunctional surface engineering, having to eliminate a brazing or welding technological step. This study investigates the laser cladding process parameters, related single track geometry and quality of multi-material samples. The optimal process parameters for steel were found of 0.21-0.26 J/mm^2 and $0.25 \cdot 10^{-2}$ g/mm under the scanning velocity of 1400-1700 mm/min and powder feeding of 4.2-4.5 g/min. The bimetal thin walls, cylinders and cubes were manufactured within the optimal conditions. The requirements of steel and nickel joining were explored. For the examination, the optical microscopy, SEM, EDX microelement analysis and hardness analysis were involved.

Peer-review under responsibility of the Bayerisches Laserzentrum GmbH

Keywords: laser cladding; multi-material; additive manufacturing; bimetal; steel; nickel alloy; Peclet number, thermal power

1. Introduction

The main purpose of engineering technology science is to achieve a predetermined quality of the product with efficient use of production facilities and resources. In these terms, the best efficiency of some engineering structures could be obtained by applying the components combined of several dissimilar materials that fully realize the economic and performance advantages of each material. The most known metal couples are as follows: steel-copper, steel-aluminum, steel-titanium and steel-nickel. For example, the pair of steel-copper (bronze) could be applied as the heat exchangers (due to high conductivity of copper/bronze) or as cam bushing (high tribological properties of

* Corresponding author. Tel.: +7-499-972-9494 ; fax: +7-499-973-3167 .
E-mail address: d.kotoban@stankin.ru

Peer-review under responsibility of the Bayerisches Laserzentrum GmbH
doi:10.1016/j.phpro.2016.08.066

copper/bronze), the pair of steel-aluminum could be applied as adapters in oxygen regenerators or as details of electrolytic refining equipment (high corrosion resistance of aluminium). Some of the examples are presented in the previous works [1-5].

Choi et al. [6] showed the steel-nickel parts used in light water reactors to connect vessel and generator nozzles to the reactor components. Ramkumar et al. [7] investigated a GTA welding of the nickel superalloy and SS304 for high temperature and corrosive environments applications such as power plants and also studied the weldability of Inconel 718 and AISI 316L [8]. Malakhov et al. [9] studied the explosion weld of nickel and steel plates for application with high temperature and high erosion load in gas turbines.

In this paper, the stainless steel and nickel alloy was chosen because of specific properties of each material: corrosion resistance of structural steel and high-temperature strength of nickel alloy. The definite part is cylindrical Ø20 mm solenoid valve consisted of soft magnetic alloy core and symmetrically located in transversal direction steel and nickel elements. The part is operated in corrosion high temperature environment. The main goal is to eliminate the brazing procedures and the related mechanical edge preparation. In this regard, the multi-material additive manufacturing was involved.

There are some researches on the multi-material additive manufacturing. For example, Liu et al. [3] showed the Selective laser melting of steel-copper bimetallic objects. The authors achieved very good metallurgical bonding even though they make an important note about some technological problems and strong need of correct process parameters. Beal et al. [10] applied the multi-material manufacturing by selective laser melting to produce functionally graded materials in XY-plane using specific powder hopper. The authors investigate the manufacturing process of injection mould made from H13 steel and copper. Yakovlev et al. [11] and Muller et al. [12] studied the multi-material laser cladding of steel 316L and Co-base superalloy from practical and theoretic point of view. Multi-material object manufacturing will meet the problems with geometry, different layer thickness for each material, needs of taking into account the difference in thermal and physical properties. Different aspects of parametric studies of the laser cladding was investigated previously [13-15], the experience of powder-gas flow and preheating was showed in [16]. Gusarov et al. [17] showed the need of input power control to avoid additional residual stresses.

The major goal of the present study was to investigate of the laser-matter interaction process using different approaches. For the study, two powders (stainless steel and nickel superalloy) of industrial use were applied. The subject was connected with the developing of optimal process parameters of laser cladding for both selected materials and fabrication of multi-material (bimetal) samples. The influence of the cladding parameters on the track geometry, microstructures and microhardness was studied. The boundary effect of small of 200 μm of laser beam diameter comparable by order-of-magnitude with powder size (50 μm) was highlighted and the thermodynamic conditions were described.

2. Materials and experimental procedure

2.1. Materials

The stainless steel and nickel superalloy powders materials were used for the study. The stainless steel powder PR-12H18N9T was produced by JSC Polema (Russia), is an austenitic stainless steel with up to 0.12% of carbon, up to 18% of chromium, up to 9% of nickel and up to 0.8% of titanium, similar to AISI321 steel. The element composition is presented in the table 1. The stainless steel powder fraction was of 20 – 63 μm (fig. 1a) with almost spherical particle shape (fig. 3a). Mean powder particle size was 40 μm. Spherical shape factor of the particles is 0.7 based on the statistical analysis software (Occhio S.A., Belgium) using the *Circularity* and *Bluntness* parameters. The measured powder bulk density without taping was 4680 kg/m^3. The steel is well established in the applications with temperatures of -196 °C to 600 °C, weak acid environment (up to 350 °C), for the parts under pressure.

The nickel powder HN71MTYuB was produced by JSC VILS (Russia) is a high-temperature nickel superalloy contains 13-16% of chromium, 2.8-3.2% of molybdenum, 2.35-2.75% of titanium, 1.45-1.8 of aluminum doped with 2% of niobium and 0.01% of cerium. Detailed element composition is presented in table 2. The granulometry of the powder is -70 μm (fig. 1b). Mean powder particle size is 55 μm. The powder presents spherical shape (fig. 3b). Spherical shape factor of the nickel powder particles is 0.8. The measured powder bulk density without taping was 5049 kg/m^3. The typical use of nickel superalloys are the application with high temperatures as turbine parts.

The granulometric analysis (fig. 1) of the powders was carried out by an optical granulomorphometer Alpaga 500 Nano (Occhio S.A., Belgium) with statistic image analysis software. The morphologic and element analysis was done by Vega 3LMH (Tescan, Czech Rep.) scanning electron microscope (SEM) equipped with energy-dispersive X-ray micro analyser (XCITE Oxford instruments). The element analysis as incoming control (table 1, 2) concerned only "heavy" components, since light elements such as carbon, oxygen, nitrogen, etc. cannot be reliably determined using EDX.

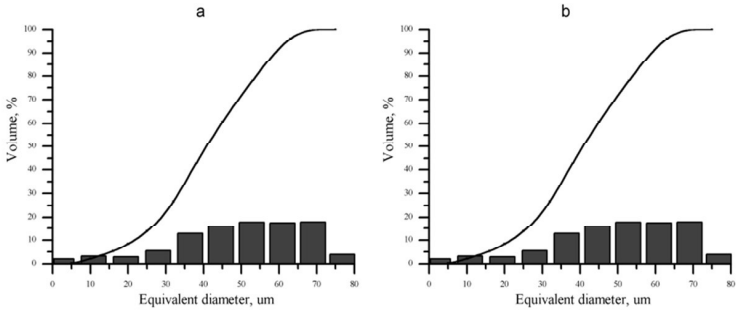

Fig. 1. Granulometry of the powders: (a) steel powder, (b) nickel powder.

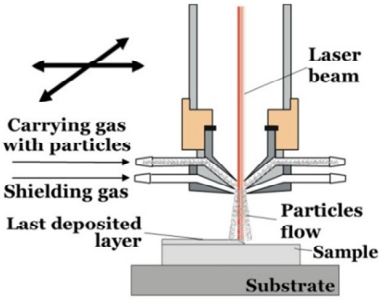

Fig. 2. Scheme of the 3D laser cladding process. The arrows show the directions of axis movement.

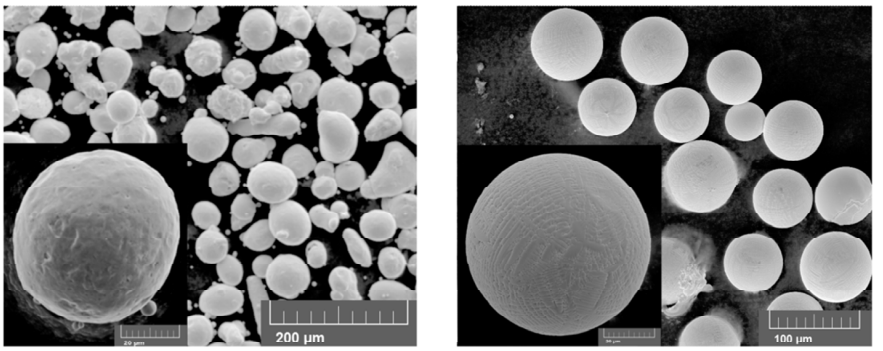

Fig. 3. SEM micrographs of the powders: a) steel powder, b) nickel powder.

Table 1. Element composition of stainless steel powder.

Element	Fe	C*	Si	Mn	Ti	Cr	Ni	S*	P*	H_2O*
PR-12H18N9T	balance	0.1	0.68	0.9	0.92	17.1	9.7	0.01	0.03	0.022

Table 2. Element composition of nickel powder.

Element	Ni	C*	Cr	Co	Mo	Al	Ti	W, Si, Mn	Nb	V	Fe	S*	P*	Cu	O_2*	N_2*
HN71MTYuB	Bal.	0.030	14.9	0.03	3.03	1.64	2.50	0.01	2.14	0.022	0.05	0.007	0.015	0.04	0.0071	0.0016

* - the elements data are provided by the manufacturer.

The powders were dried by heating up to +100 °C during 2 to 4 hours before cladding. The cladding was done on the low carbon steel. The substrates were cleaned with alcohol and sandblasted.

2.2. Experimental setup

The cladding was done using 3D CNC machine TruCell 3008 (Trumpf, Germany) equipped with Yb:YAG disc laser of 80 – 2000 W of output power with a wavelength of 1030 nm. The specific laser cladding head with coaxial powder feeding (fig. 2) was used with 7 mm standoff distance of the nozzle. The used 2-chanel powder feeding system allows applying two powders sequentially or simultaneously. The powder was supplied in the working zone through the nozzle with help of the argon shielding gas and helium as the carrying gas at the rate of 10 l/min each.

The optical system provides Ø200 μm of focused laser spot. As the purpose was to make the precision laser cladding for 3D-objects manufacturing, the experiments were done using 200 μm diameter. The transversal energy distribution inside the laser beam was almost Gaussian (TEM_{00}).

2.3. Experimental approach

The experimental way of process parameters optimization was chosen and the experimental plan was composed. First step was to produce the simplest elements of cladding i.e. single-tracks. The preliminary experiment was conducted with the following parameters: scanning velocity of 100 to 400 mm/min, 200 to 800 mm/min and 300 to 1200 mm/min for 100, 200 and 300 W of laser power respectively. The powder feeding was 0.6, 1.9 and 4.4 g/min for steel powder and 0.6, 2.0 and 4.7 g/min for nickel powder.

The following experiments were done to precise the optimal regimes. The second experiments was done using 80 W of laser power, 1000 – 3000 mm/min and 2.5, 4.4 and 5 g/min for steel and 2.7, 4.7 and 6.5 g/min for nickel powder. Some optimization was done during one-layer and multilayered objects cladding. Additional experiments were conducted with velocities up to 6000 mm/min (the maximum possible on the distance of 40 mm of track).

For the formalization of the optimization process, the combined parameters were used: the specific laser energy input E_L, J/mm^2, specific laser energy E_G, J/g and specific powder feeding F_G, g/mm (equations 1, 2, 3, where P is a laser power, V is a scanning velocity and G is a powder feed). The combined parameters could show the correlation between the number of the parameters influenced the process and the results of cladding. In this study, the specific laser energy input was 5 to 0.1 J/mm^2, specific laser energy 320 to 12 J/g, specific powder feeding was $4 \cdot 10^{-2}$ to $2 \cdot 10^{-3}$ g/mm.

$$E_L = \frac{P}{d \cdot V} = \frac{W}{mm \cdot {mm}/{min}} = \frac{J}{mm^2} \tag{1}$$

$$E_G = \frac{P}{G} = \frac{W}{{g}/{min}} = \frac{J}{g} \tag{2}$$

$$F_G = \frac{G}{V} = \frac{{g}/{min}}{{mm}/{min}} = \frac{g}{mm} \tag{3}$$

To control the geometry, the aspect ratio coefficient AR was used where the H is the height of the single-track (in cross-section) and W is the width of the single-track (equation 4). Usually, appropriate aspect ratio coefficient is in the range of 0.1 to 0.3 that ensure the best one after another single-track laying. In this study, some tracks were considered as appropriate with AR from 0.1 to 0.75.

The coefficient of mixing of cladded material with the substrate material was considered as it equation 5 presents, taking into account the areas of the clad F_{clad} and substrate F_{subs} zones. The F_{clad}+ F_{subs} is the overall visible melted zone including a clad and the mixing zone in the substrate part.

$$AR = \frac{H\ (height)}{W\ (width)} \tag{4}$$

$$\gamma = \frac{F_{subs}}{F_{clad} + F_{subs}} \cdot 100\% \quad (5)$$

2.4. Sample characterization

To control the geometry and structure of the samples the metallographic samples were prepared in usual way. The specimens were subjected to the etching using the following solutions: a) $FeCl_3$: HCl : ethanol in ratio 5g:20ml:100ml, b) glycerol : HNO_3 : HCl in volume ratio 10:10:15, c) acetic acid : HNO_3 : HCl in volume ratio 30:10:20, that were used for both materials. The optical microscope Olympus BX51 (Japan) and SEM were used to the metallographic analysis. The element analysis of the samples was determined by SEM-EDX. The hardness analysis was conducted using Vickers hardness tester Q10A (Qness, Austria).

3. Results and Discussion

3.1. Macrostructure

Experiments were conducted in three steps including process parameters optimization. The first step experiment was to define the cladding process parameters limits. The number of tracks was obtained for steel (fig. 4) and nickel (fig. 5) powders. The problem of the both powders was the very large dilution for many process parameters. Even if scanning velocity was very high the dilution became a problem that could be seen at the process diagrams for steel (fig. 6a) and nickel (fig. 6b) powders. More definitive, the problem is due to the high value of power density that is strongly depended on the small beam diameter and technological inability to reduce the power lower than 80 W. It has brought additional problems of parameters optimization due to the narrow window of optimal technological regimes that could be seen from fig. 6 a,b. The lines on the fig. 6 a,b traverse different zones of track quality because statistically there was successful and unsuccessful tracks with very similar process parameters. The figures 6 show large range of process parameters for single-track producing. For both materials some tracks were produced at the scanning velocities up 6000 mm/min.

As the laser power absorbing take place during about 10 ps in a very thin (about 20 nm) skin layer, the laser power has the higher value of importance during the process in comparison with the scanning velocity and powder feed rate (characteristic time is in ms). Taking in account the fact that with increasing of velocity the specific powder feeding reduces, i.e. the portion of the energy absorbed by powder reduces and the portion of energy absorbed by substrate increases, hence it appears that high laser power is the main reason of the dilution phenomena.

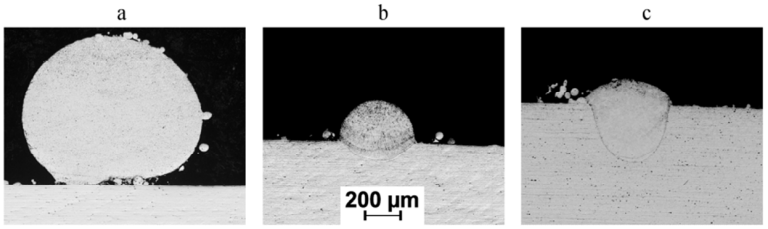

Fig. 4. Optical microscopy photos of a stainless steel tracks: (a) not enough laser energy, (b) successful geometry, (c) great dilution.
(a) P=100 W, V=100 mm/min, G=2.5 g/min; (b) P=100W, V=100 mm/min, G=0.7 g/min; (c) P=200W, V=800mm/min, G=4.4 g/min.

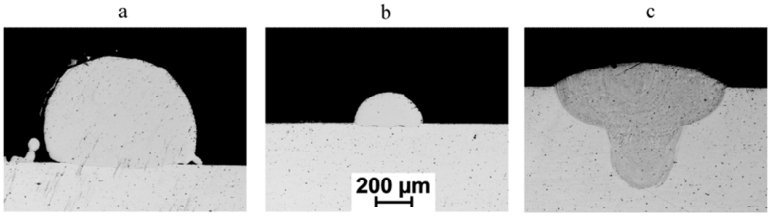

Fig. 5. Optical microscopy photos of a nickel tracks: (a) not enough laser energy; (b) successful geometry; (c) great dilution.
(a) P=100W, V=400 mm/min, G=2.7 g/min; (b) P=100W, V=100 mm/min, G=0.7 g/min; (c) P=300W, V=1200 mm/min, G=2.7 g/min.

It has to be underlined, that with both powders some single tracks were successfully produced even with 6000 mm/min of scanning speed (at 80 W and about 6 g/min i.e. about 1.2 J/g). Taking into account the described above information it could be concluded that the scanning velocity independent role. Fig. 7 presents a range of single-tacks produced with stainless steel powder with different process parameters (the experiments where E_G was more than 8 as well as scanning velocities was more than 3000 mm/min were rejected). The process parameters optima could be considered in the range of 1600 to 2100 mm/min (marked on the figure). It could be clearly visible that with similar specific laser energies E_G the meltpool decrease with scanning velocity increasing that could be connected with specific powder feeding F_G decreasing. The track cross-section is sensitive to the scanning velocity changing. It is obvious that with the scanning velocity changing the thermodynamic conditions of the process vary.

In this study, the very known Peclet number P_e was used to analyze the thermodynamic conditions of the process (equation 6) where V is scanning velocity, d is the laser beam diameter and χ is the thermal diffusivity. Peclet number shows the ratio between advective and diffusive heat transfer rates i.e. simply between mass heat transfer mechanism and thermal diffusion. In this study, the assumption of powder mass flow as a base of advective heat transfer is used.

$$Pe = \frac{V \cdot d}{\chi} \tag{6}$$

Previously, Gusarov [18] and Hoadley [19] used the Peclet number for laser additive manufacturing processes but without considering from the technological point of view. The thermal-physical properties were taken for similar materials (stainless steel 310 and 74%-nickel superalloy type Inconel 600) [20, 21] at the temperature of 1000 °C. It is to note, that the thermal diffusivity for both materials is similar: 5.7 $mm^2 \cdot s^{-1}$ for stainless steel and 5.8 $mm^2 \cdot s^{-1}$ for nickel alloy. Table 3 and 4 present the Peclet number as a function of scanning velocity.

Table 3. Peclet number vs. scanning velocity for stainless steel powder.

Scanning velocity	100	300	500	900	1300	1700	2000	2300	2600	3000
P_e	0.06	0.18	0.30	0.54	0.78	1.02	1.20	1.38	1.56	1.80

Table 4. Peclet number vs. scanning velocity for nickel alloy powder.

Scanning velocity	100	300	500	900	1300	1700	2000	2300	2600	3000
P_e	0.06	0.18	0.30	0.54	0.78	1.02	1.19	1.37	1.55	1.79

The best found process parameters from the fig. 7 corresponds to the Peclet numbers from 1 to 1.20 (for steel) and 0.8 to 0.9 (for nickel alloy) i.e. the conditions where the advection and diffusion are almost in the balance. Low Peclet numbers leads to diffusive-conductive heat transfer mechanism that allows substrate or underlayer melting. Increased Peclet number i.e. the advective heat transfer mechanism due to the powder moving prevents the substrate melting that could be considered as low adhesion to the substrate (or to the underlayer). On the other side, to estimate the required powder melting power the equation 7 could be used as the initial approximation. In this equation, instead of mass parameter the powder flow mass feed rate *m* is used providing estimation in Watts. C_p is

the specific heat of the material and ΔT is the difference between normal and melting temperatures (1400 K for both steel and nickel superalloy materials).

$$W_G = m \cdot C_p \cdot \Delta T = \frac{g}{s} \cdot \frac{J}{g \cdot °K} \cdot °K = Watt \quad (7)$$

For this study, taking in account the engineering analysis of results, it is appropriate to use the specific heat value Cp of material at 1000 °C. The specific heat was 0.655 $J \cdot g^{-1} \cdot °K^{-1}$ for stainless steel and 0.638 $J \cdot g^{-1} \cdot °K^{-1}$ for nickel superalloy [20, 21]. The dilution height axis on the figures was intentionally limited by 200 μm as well as the laser power axis was limited by 110 W to show the difference at low power/speed. The figures 8, 9 show by X-symbols the experimental laser powers and measured dilution zone height. The square marks show the calculated powers which are typically less than experimental values. The calculated results could not be directly compared to the experimental ones but since the calculated and real results are comparable by the order, the chosen laser powers (i.e. 80 and 100 W) is the appropriate solution. Taking in account the assumptions (heat transfer, powder coefficient of efficiency and laser radiation beam absorbance were not included in the calculation), it could be concluded that the estimated (calculated) value of power is oversized that is proved by the experimental data. Many of experimental tracks even with minimum laser power were with great dilution zone that could be attributed to the overheating.

In conclusion it could be highlighted that the engineering analysis by Specific energy input and Specific powder feed rate, Specific laser energy and scanning velocity, Peclet number and thermal power could be easily introduced in the optimization process of laser cladding as the useful approach.

The optimal parameters was considered as follows: a) for steel powder the specific laser input of 0.29 J/mm^2, the specific powder feed of 0.0071 g/mm and b) for nickel powder the specific laser input of 0.24 J/mm^2, the specific powder feed of 0.0063 g/mm.

Following experiments were to find the correct hatch distance. Typically the ½ of single-track width is applying as the hatch distance. During the single-layers and 3D objects process parameters optimization the parameters were slightly adjusted. The first layer typically was produced with 10% more power than the second layers that is not directly connected with multi-material cladding. For both powders it was 90 W for first and 80 W for second layers.

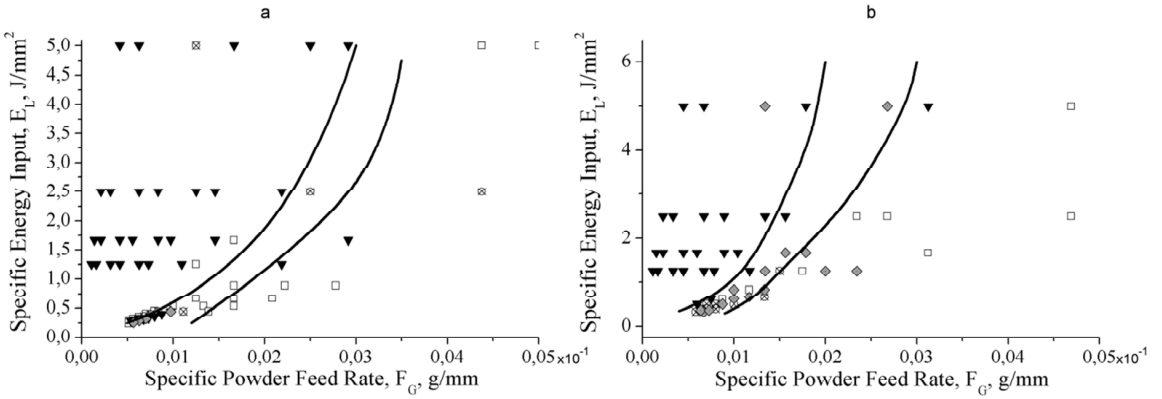

Fig. 6. Process parameters maps for steel and nickel materials: a) for stainless steel, b) for nickel.
▼ – dilution problem, ◆ - geometry irregularity, □ - dimension aspect ratio (AR) problem, ⊗ - small dilution.

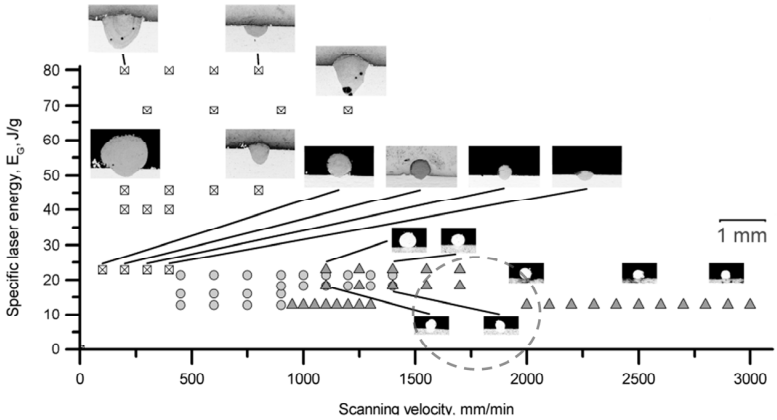

Fig. 7. The process map with parameters Specific laser energy E_G vs. scanning velocities illustrated with single-track cross-sections.

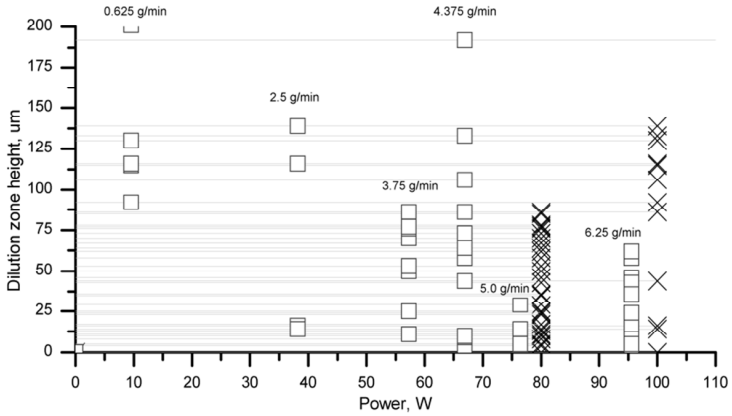

Fig. 8. The comparison of estimated power and experimental power of laser for stainless steel powder.
□ - estimated thermal power, × - experimental laser power, lines tracking the dilution from experimental values

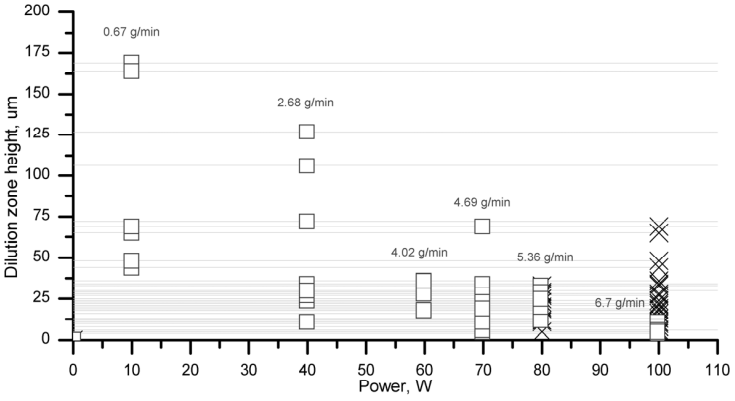

Fig. 9. The comparison of estimated power and experimental power of laser for nickel superalloy powder.
□ - estimated thermal power, × - experimental laser power, lines tracking the dilution from experimental values

a b

Fig. 10. The manufactured thin3D objects of steel-nickel bimetal: (a) walls, (b) cylinders.

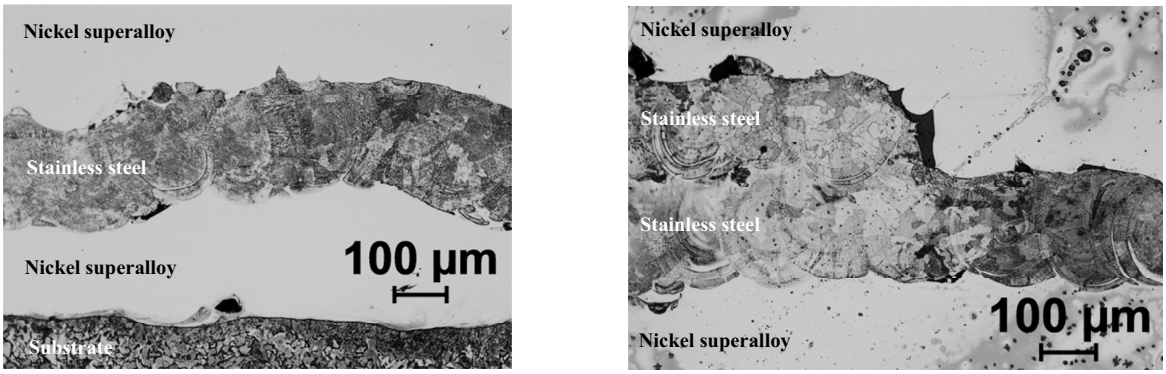

a b

Fig. 11. The cross-sections of the manufactured 3D-objects: (a) 3 layer object and (b) 4 layer object.

It is to note, that the typical width of track was about 200 to 260 μm, height was about 150 to 200 μm, for the optimal regimes. Since the optimum single-track process parameters was considered as above with the powder feed rate as high as 5 to 7 g/min the first layers were produced with these regimes. The noted problem appears as the each second single-track that was cladded in adjacent with the previous one had the great difference from the initial single-track. Since this problem was not appeared during single-track wall manufacturing, the probable explanation could be as follows. During single-track manufacturing, some powder leaves the working zone due to the gas flow dynamics and particles collisions and rebounding. In cladding of tracks to each other, the powder particles can interact with the previous track surface and return in the working zone so the overall quantity of powder involved in the cladding increases. The appropriate solution was to decrease the powder feeding rate.

This information was used in finding of hatch distances in XY and Z directions. During the work, some representative samples were manufactured (fig. 10).

3.2. Special aspects of multi-material cladding

During the experiment, the optimal hatch distances were determined when materials were fused to each other. Since the selected optimal tracks of steel and nickel were similar in geometric dimensions, there was no problem with adjusting the height of the layer. Fig. 11 presents some microphotographs of the multi-material bimetallic samples. The main remained problem is the connection between the layers and tracks. As it could be seen from the fig. 11a, the surface flatness of underlayer plays important role in the cladding of next layers. The middle steel layer

repeats the surface unevennesses. The surface is more flat at the fig. 11b. The appearing problem is the microstructural imperfections of fusing between the steel and top nickel layers. This leads to need of adjusting the cladding parameters with consideration of underlayer material due to, apparently, difference in thermal-physical properties.

The other outcome from the fig. 11b is that there is need to control the hatch distance between the steel and nickel part as well as the start point of the following cladded material. The discontinuity flaw between the second layer of steel and adjacent nickel layer could be the result of non-optimal hatch distance.

For the wall samples, the overheating at the last layers was noted. The evident reason is the changed thermal properties and conditions of laser cladding during the process. The reasonable action is to decreasing the energy input of the manufacturing of upper layers and let the material to cooling down using more dwell time between the layers manufacturing. Possible solution is to change the process parameters to make faster laser cladding using 5 to 6 m/min and more but even with 80 W of laser power, 3000 mm/min of scanning velocity and 6 to 7 g/min the track appears irregular and unstable in longitudinal direction. The other solution is to use the pulse-periodic laser regime to precise energy control. The both solutions require conducting the additional studies. The minimum achieved thickness of the wall was 260 – 350 μm (obtained by optical microscopy of the transversal section) and about 0.4 mm (by direct measurement).

The cylindrical walls (fig. 10b) were made by single tracks. The instability of the single track directly influences the morphology of the upper layer that was indicated by the wave-structure (fig. 10b, upper cylinder). The reasonable solution is to find more stable conditions of manufacturing and make an angular hatch during layer manufacturing to avoid a systematic error.

3.3. Microstructures

The transversal sections of the samples were studied by metallographic analysis. All etching solutions were applied to the cladded materials with different success. The low carbon steel substrate was etched very quickly but the cladded stainless steel needs about some minutes to dissolve the oxide layer of passivation. The results could be seen on the fig. 12. The bright field micrograph shows the grain structure and dark field micrograph shows the subgrain structure. Fig. 12a represents the grain size of about 20 to 40 μm that is typical for this type of steel. The stainless steel material represents apparently austenitic structure with columnar uniaxial dendrites with characteristic dimensions of 1.5 μm elongated in the maximum cooling heat flux direction (fig. 12b).

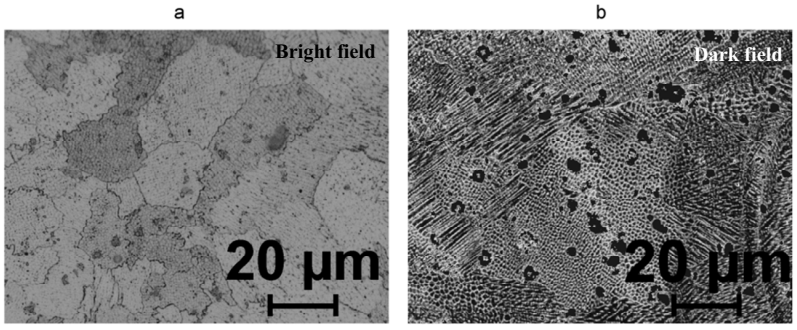

Fig. 12. The microstructure of stainless steel sample (a) in bright field and (b) in dark field.

The dark field optical microscopy allowed revealing the grain boundaries and subgrain structure of nickel base material (fig. 13a). The nickel superalloy material apparently represents γ-solid solution in fine dendritic structure with the characteristic dimensions of 1 to 3 μm (fig. 13 a,b). The more contrast image was found using oblique illumination that allows investigating the surface morphology (fig. 13 b,c). The subgrain structure was investigated and the dendritic structure could be seen more clearly. The subgrain structure of nickel alloy is slightly greater than in interface zone (fig. 13 b,c).

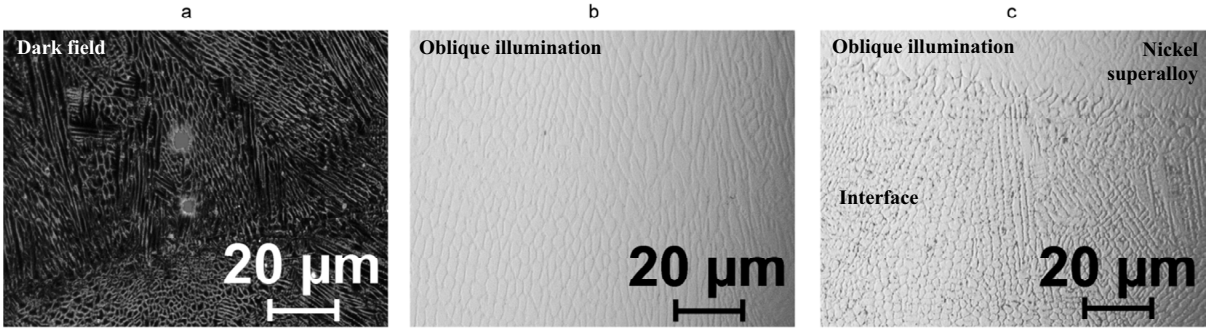

Fig. 13. The optical microscopy photos in (a) dark field and (b) oblique illumination of nickel super alloy and (c) interface between nickel and steel layer in oblique illumination.

The materials represent typical layered structure (fig. 14a). The metallurgical bonding between the layers is assured by melting a portion of bottom material (substrate or bottom layer). By the experience, the weldability of steel and nickel is good. Typically, the bottom layers was exposed to the heat flux of the cladded upper layer with the melting and heating that leads to heat treatment of material. It is appear, that this kind of steel reheating is similar to the laser quenching with semifusion or to the high tempering that homogenizes the structure with slightly increasing of grain size. The similar thermal cycle does not influence the structure of nickel super alloy.

Fusing zone of steel-nickel material represents columnar dendritic structure (fig. 13c, 14). In the experiments of layer by layer or alongside cladding, the element content was depended on the dilution. For the multitrack samples where the dilution was small the intermixing was small (fig. 14b) and for the wall-samples the intermixing was high as well as the dilution zone was great (fig. 14a). The wall-samples represent vertical columnar dendritic structure since the cooling was through the bottom wall. It also implies multiple heats during cladding of upper layers and heat accumulation.

For both materials porosity and cracking susceptibility were not observed. Since the process was conducted in the shielding atmosphere, the contamination of the melt pool by the air gases was kept to a minimum. For both materials the embrittlement is not typical.

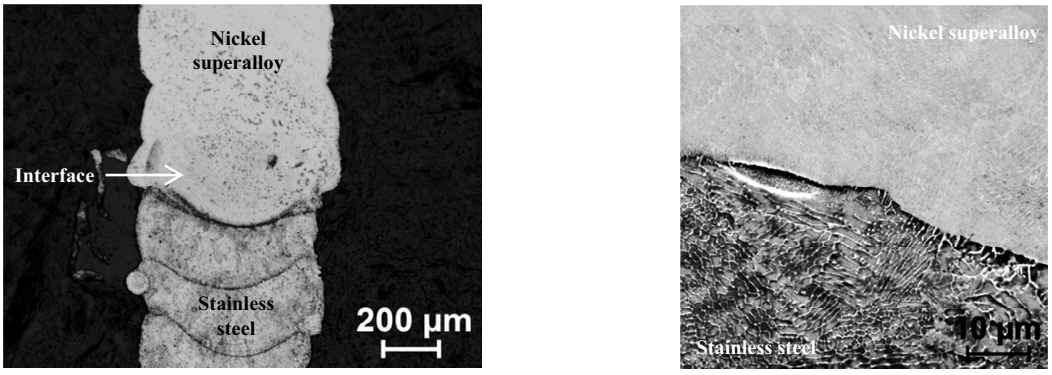

a b

Fig. 14. The interface zone of bimetal steel-nickel object: (a) an optical microphotograph of the wall sample, (b) SEM image of interface.

3.4. Element composition

The element analysis of the each cladded material showed almost initial composition. The sideview of the steel samples presented the “gold” colour that could be attributed to the titanium segregation to the surface and its nitriding by the air. The SEM-EDX study did not reveal any changes at the close to the side surface zones, but it

should be noted that the electron spot was about hundreds of nm. Apparently, the segregation did not influence to the overall element composition of the sample (and surface functionality). The element analysis along the wall was done (fig. 15) that determined the interface dimension of about 100 to 150 μm.

3.5. Hardness

The hardness analysis was done in order to evaluate the mechanical properties of the clads. The wall sample was analysed along the height (fig. 16) with the following results: 270 HV0.1 of nickel superalloy, 245 HV0.1 of the steel and about 190 HV0.1 of the substrate.

All the tracks were analysed as well. The maximum hardness of steel material was 250 HV0.1, and of nickel alloy was 350 HV0.1. The difference in the values could be attributed to the different phases. It could be pointed, that the stainless steel in the HAZ has increased microhardness apparently due to the specific heat treatment.

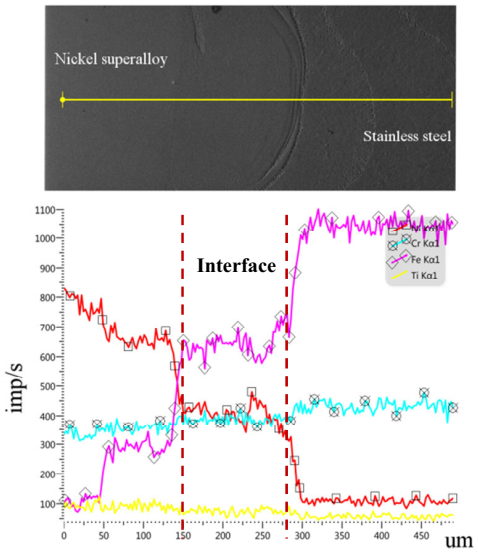

Fig. 15. Element distribution at the interface of steel-nickel bimetal. ◇ is Fe, □ is Ni, ⊗ is Cr, w/o mark is Ti.

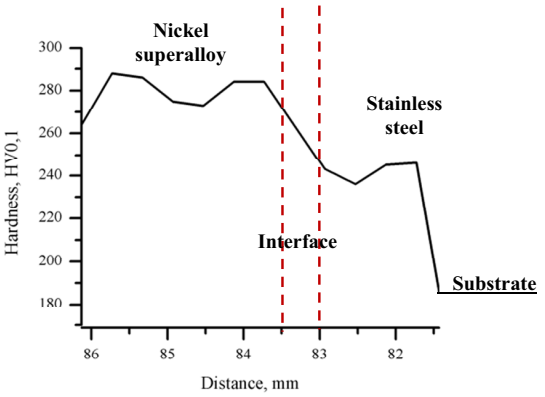

Fig. 16. Microhardness of the wall sample.

4. Conclusion

In this study, the multi-material bimetal structures from stainless steel and nickel superalloy was manufactured and the conditions of additive laser cladding were investigated. The achieved thickness of the bimetal wall was 0.4 mm, and the interface zone was less than 150 μm. The technology aspect, microstructures, element analysis and hardness analysis was done to characterize the samples. The main conclusions could be assembled as follows:

- the better power control regime is needed, for example, pulse-periodic regime of laser;
- some pairs of combined parameters and thermodynamic characteristics were proposed to investigate the process parameters optimization;
- optimum cladding process parameters for powders with similar thermal and dimensional properties are similar but the resulting clads and claddability are different;
- the power plays dominant role in the process parameters of laser cladding that was more evident with high power density beam;
- during the 3D objects manufacturing of thin-walled structures, it is required to use the quality criteria of thin-walled object in regard of its thermal state;

- in some cases during the cladding the tracks each to other, the decreasing of powder feeding rate is needed due to changes in powder distribution conditions.

The future works shall be intended to improve the process parameters (in terms of overheating of material, powder feeding distribution and in-flight melting), to control the process by optical diagnostic means and to investigate the solution on the process stabilization.

Acknowledgements

This work has been financed by the Ministry of Education and Science of the Russian Federation in the frame of governmental task in the field of scientific activities (task order No. 11.874.2014/K). The authors are deeply grateful to Dr. Prof. Gusarov whose suggestions and discussion had significant effect on quality of this work.

References

1. Shanmugarajan, B., Padmanabham, G. (2012). Fusion welding studies using laser on Ti–SS dissimilar combination. *Opt Laser Eng*, *50*(11), 1621-1627.
2. Gnyusov S. F., Orishich A. M. (2012) Structurally-phase state and mechanical properties of welded joints in laser welding of titanium and stainless steel [In Russian: Strukturno-fazovoye sostoyaniye i mekhanicheskiye svoystva svarnykh soyedineniy pri lazernoy svarke titana i nerzhaveyushchey stali], *Izv. Tomskogo politekh.o univ*. *321*(2), 94-99.
3. Liu, Z. H., Zhang, D. Q., Sing, S. L., Chua, C. K., Loh, L. E. (2014). Interfacial characterization of SLM parts in multi-material processing: Metallurgical diffusion between 316L stainless steel and C18400 copper alloy. *Mater Charact*, *94*, 116-125.
4. Gomez, X., Echeberria, J. (2003). Microstructure and mechanical properties of carbon steel A210–superalloy Sanicro 28 bimetallic tubes. *Mater Sci Eng: A*, *348*(1), 180-191.
5. Weigl, M., Schmidt, M. (2009). Modulated laser spot welding of dissimilar copper-aluminum connections. *Proceedings of 4M/ICOMM conference, 4*, 211-214.
6. Choi, K. J., Kim, J. J., Lee, B. H., Bahn, C. B., & Kim, J. H. (2013). Effects of thermal aging on microstructures of low alloy steel–Ni base alloy dissimilar metal weld interfaces. *J Nucl Mater*, *441*(1), 493-502.
7. Ramkumar, K. D., Arivazhagan, N., Narayanan, S., Mishra, D. (2014). Hot corrosion behavior of monel 400 and AISI 304 dissimilar weldments exposed in the molten salt environment containing Na2SO4+ 60% V2O5 at 600° C. *Mater Res*, *17*(5), 1273-1284.
8. Ramkumar, K. D., Patel, S. D., Praveen, S. S., Choudhury, D. J., Prabaharan, P., Arivazhagan, N., Xavior, M. A. (2014). Influence of filler metals and welding techniques on the structure–property relationships of Inconel 718 and AISI 316L dissimilar weldments. *Mater Design*, *62*, 175-188.
9. Malakhov, A. Y., Perbukhin, L. B., Saikov, I. V., Vikhman, V. B. (2015). Explosion welding of high-strength bimetallic materials with a cladding layer based on niobium and nickel–cobalt alloys. *Weld Int*, *29*(10), 805-808.
10. Beal, V. E., Erasenthiran, P., Ahrens, C. H., Dickens, P. (2007). Evaluating the use of functionally graded materials inserts produced by selective laser melting on the injection moulding of plastics parts. *P I Mech Eng B-J Eng*, *221*(6), 945-954.
11. Yakovlev, A., Trunova, E., Grevey, D., Pilloz, M., Smurov, I. (2005). Laser-assisted direct manufacturing of functionally graded 3D objects. *Surf Coat tech*, *190*(1), 15-24.
12. Muller, P., Mognol, P., Hascoët, J. Y. (2013). Modeling and control of a direct laser powder deposition process for Functionally Graded Materials (FGM) parts manufacturing. *J Mat Process Techn*, 213(5), 685-692.
13. Grigor'ev, S. N., Tarasova, T. V., & Gvozdeva, G. O. (2016). Optimization of Parameters of Laser Surfacing of Alloys of the Al–Si System. *Met Sci Heat Treat*, *57(9)*, 589-595.
14. Farahmand, P., Kovacevic, R. (2014). Parametric study and multi-criteria optimization in laser cladding by a high power direct diode laser. *Laser Manuf Mater Process*, *1*(1-4), 1-20.
15. Kotoban, D. V., Shishkovskii, I. V. (2016). A Study of the Structure of Nickel Aluminide After Laser Treatment. *Met Sci Heat Treat 57(9)*, 603-609.
16. Kovalev, O. B., Zaitsev, A. V., Novichenko, D., Smurov, I. (2011). Theoretical and experimental investigation of gas flows, powder transport and heating in coaxial laser direct metal deposition (DMD) process. *J Therm Spray Techn*, *20*(3), 465-478.
17. Gusarov, A. V., Pavlov, M., Smurov, I. (2011). Residual stresses at laser surface remelting and additive manufacturing. *Physics Procedia*, *12*, 248-254.
18. Protasov, C. E., Gusarov, A. V. (2015). Modeling the Effect of Beam Shaping at Selective Laser Melting. *Materials Science Forum. 834,* 85-92.
19. Hoadley, A. F. A., Rappaz, M. (1992). A thermal model of laser cladding by powder injection. *Metallurgical Transactions B, 23(5),* 631-642.
20. Blumm, J., Lindemann, A., Niedrig, B., Campbell, R. (2007). Measurement of selected thermophysical properties of the NPL certified reference material stainless steel 310. *International journal of thermophysics, 28(2),* 674-682.
21. Blumm, J., Lindemann, A., & Niedrig, B. (2003). Measurement of the thermophysical properties of an NPL thermal conductivity standard Inconel 600. *Proc. of 17th European Conference on Thermophysical Properties*. 621-626.